This is the accepted manuscript version of the contribution published as:

The publisher's version is available at:

1 **Correlative imaging of the rhizosphere – A multi-method workflow**

2 **for targeted mapping of chemical gradients**

3

4 Eva Lippold[1] *, Steffen Schlüter[1], Carsten W. Mueller[2, 3], Carmen Höschen[2], Gertraud

5 Harrington[2], Rüdiger Kilian[4], Martina I. Gocke[5], Eva Lehndorff[6], Robert Mikutta[7],

6 Doris Vetterlein[1,7]

7

8 [1] Department of Soil System Science, Helmholtz Centre for Environmental

9 Research – UFZ, Theodor-Lieser-Straße 4, 06120 Halle (Saale), Germany

10 [2] Technical University of Munich, TUM School of Life Sciences, Department of Life

11 Science Systems, Soil Science, Emil-Ramann-Str. 2, 85354 Freising, Germany

12 [3] University of Copenhagen, Department of Geosciences and Natural Resource

13 Management, Øster Voldgade 10, 1350 Copenhagen, Denmark

14 [4] Mineralogy and Geochemistry, Martin Luther University Halle-Wittenberg, Von-

15 Seckendorff-Platz 3, 06120 Halle (Saale), Germany

16 [5] Soil Science and Soil Ecology, Institute of Crop Science and Resource

17 Conservation, University of Bonn, Nussallee 13, 53115 Bonn, Germany

18 [6] Soil Ecology, Bayreuth University, Dr.-Hans-Frisch-Str. 1-3, 95448 Bayreuth,

19 Germany

20 [7] Soil Science and Soil Protection, Martin Luther University Halle-Wittenberg, Von-

21 Seckendorff-Platz 3, 06120 Halle (Saale), Germany

22

1

23 *Corresponding author:*

24 Eva Lippold, eva.lippold@ufz.de; phone +49 3455585422

25

Abstract

30 Examining *in-situ* processes in the soil rhizosphere requires spatial information on

31 physical and chemical properties under undisturbed conditions. We developed a

32 correlative imaging workflow for targeted sampling of roots in their 3D context and

33 assessing the imprint of roots on chemical properties of the root-soil contact zone at

34 μm to mm scale. Maize (*Zea mays*) was grown in ^{15}N-labelled soil columns and

35 pulse-labelled with $^{13}CO_2$ to visualize the spatial distribution of carbon inputs and

36 nitrogen uptake together with the redistribution of other elements. Soil columns were

37 scanned by X-ray computed tomography (X-ray CT) at low resolution (45 μm) to

38 enable image-guided subsampling of specific root segments. Resin embedded

39 subsamples were then analysed by X-ray CT at high resolution (10 μm) for their 3D

40 structure and chemical gradients around roots using micro X-ray fluorescence

41 spectroscopy (μXRF), nanoscale secondary ion mass spectrometry (NanoSIMS), and

42 laser-ablation isotope ratio mass spectrometry (LA-IRMS). Concentration gradients,

43 particularly of calcium and sulphur, with different spatial extents could be identified by

44 μXRF. NanoSIMS and LA-IRMS detected the release of ^{13}C into soil up to a distance

45 of 100 μm from the root surface, whereas ^{15}N accumulated preferentially in the root

46 cells. We conclude that combining targeted sampling of the soil-root system and

47 correlative microscopy opens new avenues for unravelling rhizosphere processes *in*

48 *situ*.

Synopsis

50 Chemical mapping of the rhizosphere in three dimensions remains a methodological

51 challenge. Our novel imaging workflow allows for targeted root sampling and

52 chemical analysis, successfully studying rhizosphere processes *in situ*.

1. Introduction

54 Roots as an essential part of plants perform essential functions such as anchoring

55 the plant to the soil [1] and absorbing water [2] and nutrients [3]. The zone of soil affected

56 by roots can be defined as the rhizosphere [4]. Most of our knowledge on rhizosphere

57 properties is based on operationally defined ways of sampling the rhizosphere, such

58 as brushing, shaking, or washing off soil adhering to the roots after extracting them

59 from bulk soil. These approaches do not refer to a certain distance from the root

60 surface, although nutrient gradients are reported to extend over less than one mm up

61 to several cm [5–8]. Furthermore, destructive rhizosphere samples can be

62 contaminated with root cells i.e. root hairs being also brushed off [9]. Current

63 knowledge with respect to chemical gradients in rhizosphere soil has primarily been

64 based on systems not considering the radial geometry of transport to and from roots

65 such as rhizobox or split-compartment experiments. Not accounting for this geometry

66 in planar experimental setups leads to an amplification of the extent and magnitude

67 of gradients [10,11]. In addition, chemical gradients change with time of interaction [12]

68 and depend on root type and age [13,14] as well as soil texture and mineral

69 composition. Therefore, both factors (soil and roots properties) are supposed to be a

3

70 crucial parameter for the extent of physical and chemical gradients [15]. Soil properties

71 can be quantified *ex situ* whilst root age and root type can hardly be assessed by

72 conventional methods in pot experiments due to opaque soil. Both properties are

73 accessible by repeated non-invasive imaging [16,17] which can be combined with

74 subsequent 2D-chemical imaging to acquire information in 3D context. Currently,

75 most chemical and biological microscopy techniques in intact soil can only be

76 performed on exposed soil surfaces within two-dimensional soil surfaces. This

77 introduces severe biases since spatial information outside of the imaging plane is

78 unavailable [18], including all roots that are out of plane. For this reason, there is a

79 need for methods that combine 3D structural information with 2D biochemical

80 information to integrate this spatial context. This so-called image registration or co-

81 registration has been demonstrated for combinations of 3D X-ray computed

82 tomography (X-ray CT) with several different techniques such as scanning electron

83 microscopy (SEM) coupled with energy-dispersive X-ray spectroscopy to reveal

84 elemental maps [19,20], fluorescence microscopy to assess bacterial distributions [18,21],

85 zymography to unravel enzyme release patterns [22] or light and near infrared

86 spectroscopy to account for the spatial distribution of organic matter [23]. All these

87 microscopy techniques have in common that spatial resolution and mapped areas

88 roughly match the spatial resolution and cross-sectional areas captured with X-ray

89 CT. With other techniques a dimensional or scale discrepancy must first be

90 overcome before the biochemical information can be registered into the 3D spatial

91 context. This can occur because the method provides only point or line information,

92 e.g. laser ablation isotope ratio mass spectroscopy (LA-IRMS) [24] and laser ablation

93 inductively coupled plasma mass spectrometry [25]. It can also happen that 2D

94 information is only available with a tiny field of view as is the case for electron

4

95 microscopy with electron energy loss spectroscopy [26] or nanoscale secondary ion

96 mass spectrometry (NanoSIMS) [27,28]. In these cases, a two-step registration

97 approach with another microscopy technique that bridges both scales is beneficial

98 [18,29]. A successful 2D-3D image registration routine inherently demands the structural

99 integrity of a given sample during preparation and each subsequent analysis step.

100 The mentioned spectromicroscopic techniques often have common prerequisites for

101 sample preparation as samples need to be dehydrated and vacuum stable [30].

102 Likewise complex samples as for instance intact soil cores are oftentimes embedded

103 and sectioned in a resin or agar matrix to preserve the structural integrity but the

104 structural integrity before and after embedding is rarely checked [23]. Moreover, the

105 unintentional modification of chemical gradients by colloid redistribution or solute

106 leaching during sample preparation remains unclear [30].

107 The aim of the current study was to capture radial chemical gradients in the

108 rhizosphere of well-characterized 3D root segments as a result of interacting

109 processes at the interface between roots, microorganisms, and the soil matrix. To do

110 so, we established a procedure for correlative image analysis of resin-embedded

111 rhizosphere soil containing roots types of a specific age. This protocol was tested on

112 a maize column experiment involving ^{13}C- and ^{15}N-isotope labelling to trace the

113 release of plant-derived C into the soil and plant uptake of inorganic N within the

114 rhizosphere. For the first time we used targeted sampling of specific root segments

115 instead of sample extraction at pre-defined positions [31] in order to reveal the

116 formation of chemical gradients upon root growth in a 3D context. X-ray CT was

117 combined with a range of techniques (µXRF, NanoSIMS, LA-IRMS) probing different

118 chemical features of the rhizosphere (Table 1). Several methodological

119 improvements were combined to advance the information content and accuracy of

5

correlative imaging. First, the spatial context of individual root segments within the root system, i.e. root type, root order, root age, and time of interaction with the soil, was revealed by repeated whole-column X-ray CT scans prior to subsample extraction. Second, the sequence of 2D imaging techniques, each providing complementary chemical information, were assigned such that co-registration is possible and adverse effects by sample preparation are minimal. Third, the obtained 2D radial gradients are registered with 3D root distance information retrieved from X-ray CT scans of subsamples to include knowledge about roots outside of the imaging plane.

2. Materials and Methods

Growth system, X-ray CT scanning, localisation of subsamples, and sample extraction

Samples were taken from a soil column planting experiment described elsewhere [16]. Briefly, acrylic glass tubes (250 mm height, 70 mm inner diameter) were filled with a sandy substrate which consists of a mix of 83.3% quartz sand (WF 33, Quarzwerke Weferlingen, Germany) and 16.7% of sieved loam obtained from the upper 50 cm of a haplic Phaeozem soil profile [4]. Fertilisation with a combination of unlabelled and isotope-labelled fertiliser was done prior to filling the columns. To trace the fate of inorganic N, ^{15}N was applied as $NH_4{}^{15}NO_3$ (98 atom%, Euriso-Top GmbH, Germany) at a dose of 50 mg N kg^{-1} together with the basal fertilisation of all other essential nutrients. Growth of *Zea mays* took place over a time period of 21 days under controlled conditions in a climate chamber, which was set to 22°C during the day and 18°C at night with a 12 h light period, 350 µM m^{-2} s^{-1} photosynthetically active

6

143 radiation, and a relative humidity of 65%. At day 21, plants were pulse labelled in ^{13}C-

144 enriched atmosphere to trace the fate of assimilated C. Gas tight chambers covering

145 eight plants were set up and $^{13}CO_2$ (Na$_2$^{13}CO$_3$, 99 atom%, Euriso-Top, Germany)

146 was released by adding sulfuric acid to the initial solution of sodium carbonate and

147 200 ml water following a protocol adapted from Heinrich et al. [32]. The second $^{13}CO_2$

148 pulse was performed 2 hours after the first pulse without opening the chambers in

149 between. Each pulse added 2030 ppmv CO_2 to the atmosphere; chambers were

150 removed after the full light period of 12 h.

151 In order to follow root development, X-ray CT scanning was performed at day 7, 14,

152 and 21 after planting during the night to not interfere with plant photosynthesis in the

153 same way as described by Lippold et al. [16]. A lead shield was also placed between X-

154 ray source and the soil column to shield the plant shoot and the soil outside the field

155 of view. With this setup, the dose per scan in the centre of the column amounts to 1.2

156 Gy [33]. The obtained whole-column images with a resolution of 45 μm [16] were used

157 during sampling to allow for a targeted sampling of specific root types and root ages

158 (Fig. 1a). In this study, a sample was selected that featured a primary root which was

159 at least 14 days old and which included several laterals of the same age.

160 Aluminium rings with a wall thickness of 0.25 mm and 16 mm inner diameter

161 and height were used for sampling, further on referred to as 'subsamples' (Fig. 2c).

162 The subsample dimensions have been chosen according to the following criteria: (i)

163 sufficient resolution with X-ray CT (10 μm), (ii) optimum resin infiltration, minimum

164 wall thickness to avoid compaction of the sample during insertion and, at the same

165 time, (iii) sufficient stiffness to avoid wall deformation by touching and transport, and

166 (iv) covering a size adjusted to usual sample holders during 2D imaging. A small hole

167 (1 mm diameter) was drilled into the aluminium cylinder before sampling which

7

168 always pointed into the same direction in all the following steps. The hole is visible in

169 X-ray CT scans and provides orientation during subsequent sample analyses.

170   Sampling was done with a custom-made sampling device (UGT GmbH,

171 Germany) potentially allowing for extraction of up to five subsamples from one layer

172 of the soil column (Fig. 2a). The aluminium rings were pushed into soil by moving the

173 specimen mount down or pushing the rings into the soil surface by hand. The entire

174 soil column was then pushed 20 mm upwards with a piston from below (Fig. 2a). This

175 kept the internal structure of the subsample intact, as soil compaction through

176 mechanical stress by the piston was only exerted on the opposite site of the soil core

177 and fractures along the cylinder wall were generally small. Aluminium rings can be

178 mounted such that they are pushed into the soil at predefined locations with

179 equidistant spacing (Fig. 2b). Sampling a predefined position (Fig. 2b) allows for

180 capturing the spatial heterogeneity in root and soil properties in a systematic way [31].

181 However, it requires a rather large number of samples for subsequent chemical

182 fixation and X-ray CT, as every sample has to be checked for roots and their position

183 within the sample. Alternatively, the rings can be placed freely such that the sampling

184 point on the surface of the soil column can be selected for targeted sampling of

185 individual root segments which were previously identified by whole-column X-ray CT

186 scans (Fig. 2e). This targeted sampling reduces sample numbers, the time between

187 sampling and embedding, and therefore improves the quality of each individual

188 sample.

189   After removing the subsamples by hand with a razor blade, small cavities were

190 filled up with pure quartz sand to prevent any dislocation of small particles during

191 fixation, CT scanning, and resin impregnation. Then, top and bottom of the

192 subsamples were closed with 30-µm nylon mesh and cable tie (Fig. 2c).

8

193 *Chemical fixation and embedding*

194 To stop metabolic processes in the roots and soil microorganisms as well as to

195 sustain biological cell integrity, subsamples were chemically fixated using Karnovsky

196 fixative [34]. The fixative was applied through capillary rise by placing the sample in five

197 drops of fixative from below and three onto the top of the sample. This approach

198 guaranteed sufficient fixation and at the same time caused less structural damage,

199 bubble formation, and particle relocation than full immersion into the fixative at

200 ambient pressure or even under mild vacuum (Fig. 3) [35,36]. The redistribution of

201 particles or soluble compounds by liquid movement during fixation is discussed

202 below. Fixated samples were stored at 4°C until X-ray CT analysis with a resolution

203 of 10 µm as described by Phalempin et al. [31] to have a 3D image with optimal

204 contrast of the root and the surrounding soil matrix for correlative imaging.

205 After a maximum storage time of 7 days between sampling and X-ray CT

206 analysis at 7°C in the dark, samples were dehydrated in graded acetone according to

207 the adapted method of Herrmann et al. [36]. This approach was chosen as alternative

208 to freeze-drying. In samples with these dimensions, moisture from inside did not

209 escape fast enough during drying and therefore caused structural damage upon

210 freezing. Likewise, air drying leads to a loss of root-soil contact caused by shrinkage

211 of roots and/or soil (images not shown). However, root-soil contact ought to be

212 maintained for a correct determination of the extent of chemical gradients within the

213 rhizosphere. Dehydration with a series of acetone additions, however, bears the risk

214 of washing out easily soluble compounds, which might also occur to some degree

215 during subsequent resin embedding as discussed below. The dehydrated samples

216 were embedded in Araldite 502 as described by Mueller et al. [35] and cured at 60°C

217 for 48 h until complete polymerization. A vacuum (~200 mbar below atmospheric

9

218   pressure, varying between samples was applied during the embedding procedure to

219   enhance capillary saturation and at the same time reduce dislocation of particles, as

220   repacked, unconsolidated soils have very low structural stability (Fig. 3). To keep

221   track of any particle displacement all samples were scanned again with X-ray CT,

222   using the same scanner settings as before the embedding. Note that in X-ray CT

223   scans of embedded samples roots are barely visible anymore as the electron density

224   of resin and organic material are very similar. Their position can be determined by

225   their relative position to the soil matrix known from previous scans (Fig. 3). It was

226   also possible to use epifluorescence microscopy to identify the roots in some cases

227   (images not shown) [37].

228   *Thin section preparation for chemical imaging*

229   There were several criteria for selecting the cutting plane of the embedded soil cores.

230   Despite the careful treatment of the subsamples, small air entrapments were still

231   present in the embedded samples causing small areas of displaced particles. Such

232   areas were identified by X-ray CT and disregarded for correlative microscopy. In

233   addition, some of the big roots showed some shrinkage in their cortex cells due to

234   desiccation between sampling and embedding. This shrinkage could have been

235   reduced by applying more fixative. However, this would have posed the risk that

236   chemical gradients would have been deteriorated even stronger. Based on those

237   observations and the comparison of X-ray CT images before and after embedding,

238   subsamples with minimal disturbances and a good root to soil contact were cut at a

239   targeted plane using an automatic precision saw with a diamond blade (Minitom,

240   Struers, Germany). The criteria for selecting a target plane were to cut roots

10

241 perpendicularly and select for roots with a sufficient wall distance surrounded by

242 intact soil.

243   The cut and resin-embedded subsample was cured again for 24 hours at 65°C

244 after gently removing the remaining aluminium cylinder. This drying step is very

245 important to remove water being pressed into the sample during cutting. Otherwise,

246 the sample would lose vacuum stability during subsequent imaging. Removing the

247 aluminium cylinder avoids artefacts during elemental mapping and dents and

248 scratches on the sample surface during polishing. During the whole procedure the

249 orientation of the original sample was kept to ensure the subsequent registration of

250 the different imaging approaches. After drying, the soil section was glued with a two-

251 component epoxy resin onto a glass disc of 25.4 mm diameter and cured again for

252 24 h at 65°C. Soil sections were thinned and subsequently polished manually using a

253 manual grinding and polishing machine (EcoMet30, Buehler, Germany) with diamond

254 sanding plates with increasing fineness (MD-Piano 80, 500, 1200, 2000, and 4000;

255 Struers, Germany). The sample surface was checked repeatedly under a microscope

256 to ensure whether the targeted cross section identified with X-ray CT was already

257 reached. This way it was possible to reach the targeted cross section with very high

258 precision of ± 30 µm. There is a rather narrow range of optimal soil section thickness

259 for correlative imaging. A sufficient thickness of the sample was especially required

260 for µXRF analysis to ensure to not underestimate the photon counts of heavier

261 elements with greater excitation depth, as the maxima of excitation may exceed the

262 sample thickness. The final section thickness should thus not be thinner than 25 µm.

263 For high-quality µXRF imaging it was also vital to obtain samples being perfectly

264 parallel over the full range of the thin section. Sections thicker than 100 µm also

265 compromise imaging techniques like electron microscopy and NanoSIMS due to

11

266   more intense outgassing under vacuum conditions. After the last step of polishing,

267   samples were cleaned in an ultrasonic bath in demineralised water for 30 s and then

268   dried again at 65°C for 24 h. A brightfield reflected light microscopy image

269   (AxioImager Z2, Carl Zeiss, Germany) of the whole soil section was then acquired,

270   being later used as reference image for the registration of images derived from the

271   various chemical mapping techniques.

272   *Sequence of imaging*

273   An appropriate sequence of imaging techniques has to fulfil at least two criteria: First,

274   the workflow should begin with larger scale and higher-dimensional imaging modality

275   to identify the rhizosphere and interesting transects or sites. Second, interference of

276   one imaging technique with another, e.g. by sputtering or material ablation via laser

277   shots should be minimized [30]. Based on the prerequisites of individual imaging

278   techniques (Table 1) in the current study this resulted in the following sequence: X-

279   ray CT, light microscopy, µXRF, SEM, NanoSIMS, and LA-IRMS (Fig. 1). The thinner

280   the soil section, the more reflection from the sample holder was visible in the

281   epifluorescence images (images not shown). This impaired visual root detection,

282   which was prerequisite for further measurements and the subsequent image analysis

283   steps. Alternatively, the position of roots and regions of interest for correlative

284   chemical imaging were identified in this study by jointly screening the two X-ray CT

285   images of the samples (before and after embedding) and the following µXRF images,

286   whenever roots were not directly visible.

287   *Micro X-ray fluorescence spectroscopy*

288   Elemental mapping was carried out with µXRF (Micro-XRF Spectrometer M4

289   TORNADO, Bruker). From a suite of elements that could potentially be analysed only

         12

290 results for calcium (Ca), phosphorus (P), and sulphur (S) are interpreted here, but

291 other elements like chlorine (Cl) and silicon (Si) provide valuable auxiliary information

292 for correlative microscopy. The size of the 2D region of interest was chosen such that

293 the root was in the centre and surrounded by 2.5-4 mm of soil to cover the

294 anticipated gradients based on literature [7,22,38]. Whenever exact root interfaces could

295 not be identified clearly with X-ray CT or light microscopy, a map with a short scan

296 time of the whole sample was done and the combined image of Si and Ca as well as

297 S was used to identify soil particles and roots, respectively. The settings for µXRF

298 were chosen as follows: Ag anode at 50 kV with 599 µA and 20 µm spot size, stage

299 speed of 667 µm s^{-1} equivalent to an acquisition time of 30 ms pixel^{-1}. To reduce

300 sample damage by excessive X-ray exposure, an area of interest was mapped ten

301 times at low acquisition times at higher stage speeds and these ten frames were

302 accumulated to improve count statistics. Depending on the size of the region of

303 interest and the minimum stage speed, one scan took 4 to 6 hours.

304 *Nanoscale secondary ion mass spectrometry*

305 To study the polished thin sections a scanning electron microscope (SEM; Jeol JSM

306 5900LV, Tokyo, Japan) equipped with a back-scattered electron detector (LVBED-C)

307 was used at 10 keV. Based on the SEM image, a transect from the root into the

308 surrounding soil was mapped using nanoscale secondary ion mass spectrometry

309 (NanoSIMS). The NanoSIMS images were recorded with a Cameca NanoSIMS 50L

310 (Gennevilliers, France). Prior to the NanoSIMS measurements, an Au/Pd layer (~30

311 nm) was sputter coated to avoid charging during the measurements. Additionally, the

312 electron flood gun was used to compensate for any charging effects due to the

313 nonconductive mineral particles (e.g., larger quartz grains). The Cs$^+$ primary ion

13

314   beam was used with a primary ion impact energy of 16 keV. Prior to final analysis,

315   contaminants and the Au/Pd coating layer were sputtered away at 50 × 50 μm using

316   a high primary beam current of 270 pA for 5 min (pre-sputtering). During this pre-

317   sputtering, the reactive Cs^+ ions were implanted into the sample to enhance the

318   secondary ion yields until steady state for the secondary ions is reached. The primary

319   beam (ca. 2 pA) was focused at a lateral resolution of about 150 nm and was

320   scanned over the sample, with $^{16}O^-$, $^{12}C^{12}C^-$, $^{12}C^{13}C^-$ $^{12}C^{14}N^-$, $^{12}C^{15}N^-$, $^{27}Al^{16}O^-$, and

321    $^{56}Fe^{16}O^-$ secondary ions collected on electron multipliers with an electronic dead time

322   fixed at 44 ns. The mass resolution was set to accurately detect the secondary ions

323   affected by mass interferences with their isobars. All measurements were done in

324   imaging mode with a field of view of 30 × 30 μm, 40 planes were acquired using a

325   dwell time of 1 ms/pixel, with 256 × 256 pixels. Images were corrected for electron

326   multiplier dead time and the measurements stacks were accumulated using the

327   openMIMS plugin in ImageJ [39]. The combination of all seven channels into one

328   image stack and further calculations such as image ratios and Hue-Saturation-

329   Intensity maps of any combination of isotopes were done in Fiji/ImageJ [40].

330   *Laser-ablation isotope ratio mass spectrometry*

331   Laser-ablation isotope ratio mass spectrometry was performed for probing $\delta^{13}C$

332   transects using a custom-made system equipped with a cold Nd:YAG laser (LSX-

333   213G2+, Teledyne-CETAC, Omaha, NE, USA) attached to a combustion system,

334   GC-column, ConFlo, and a Delta V isotope ratio mass spectrometer as detection

335   system [24]. Two transects across the primary root were measured over a distance of

336   200 μm extending away from the root surface as well as from the root surface into

337   the centre of the root. Each laser ablation site was set to 30 μm in diameter

14

338   corresponding to one single NanoSIMS image to compare and cross validate both

339   methods (Fig. 5b). The δ^{13}C of the ablated material was corrected daily for the δ^{13}C

340   of the CO_2 background and an acryl standard was used as reference material [24].

341   *Image registration*

342   To merge information from various imaging techniques a registration of all images

343   onto each other is necessary. Image registration of all 2D imaging techniques was

344   carried out with the ImageJ plug-in Correlia [29]. As NanoSIMS provides spatial

345   information of a very small field of view, all NanoSIMS images were first registered

346   onto SEM images (images not shown) based on electron backscattering as

347   described above. This approach provides very good contrast between mineral

348   particles, organic soil constituents, and embedding resin, thus capturing the overall

349   soil pore structure well. Thus, the largest SEM image was used to register all

350   NanoSIMS onto the reflected light microscopy image (Fig. 4b). The LA-IRMS

351   measurements were automatically combined with a camera image acquired during

352   the ablation process. This auxiliary image was used to align LA-IRMS with the light

353   microscopy images and thereby also with SEM and NanoSIMS maps. This bridging

354   via the light microscopy reference image was essential because a direct registration

355   of NanoSIMS maps and LA-IRMS spots would have been impossible. Dark patches

356   visible in the auxiliary light microscopy image before LA-IRMS (image not shown)

357   were caused by prior NanoSIMS imaging, which slightly changed the material

358   contrast. This effect was harnessed to locate target spots for LA-IRMS

359   measurements. All elemental maps retrieved with µXRF were registered with the light

360   microscopy image by means of the Si channel with very good contrast between

361   mineral particles and air-filled pores. Likewise, X-ray CT images were registered into

15

362   the µXRF Si channel by aligning the pore structure (Fig 1d, c). For registration of the

363   3D X-ray CT image into a 2D reference image we used the elastix software [41]. Image

364   registration with different dimensionality is not implemented in elastix but the 2D

365   image can be converted into a 3D image with a thickness of one slice beforehand.

366   The exact co-registration of the 2D microscopy plane with the 3D CT image can be

367   substituted by simply selecting the best matching horizontal slice, when the

368   microscopy plane was not tilted by more than three times the voxel resolution during

369   gluing, cutting, and polishing.

370   *Image analysis*

371   A prerequisite for quantitative image analysis is image segmentation of grayscale

372   data into material classes. Root segmentation of the whole-column and subsample

373   X-ray CT scans was carried out with a modified version of the root segmentation

374   algorithm "Rootine v.2" [31]. Elastix was also used to register root images after 7, 14

375   and 21 days with each other in order to generate composite images of root age (Fig.

376   1a). Resin and root segmentation in X-ray CT or µXRF data was carried out with the

377   default thresholding method in ImageJ. By using the µXRF image of the chlorine

378   channel, pores filled with resin were segmented as the resin contains traces of

379   chlorine. Roots and resin-filled pore space were separated using supervised

380   segmentation in ImageJ. Root distances in soil were retrieved with the Euclidean

381   distance transform of binary root images in ImageJ. This was either done directly in

382   the 2D microscopy image or in 3D CT images, and the resulting 3D distance maps

383   were subsequently registered into the microscopy plane, thus accounting for

384   potentially shorter distances to roots outside of the microscopy plane (Fig. 5c).

385   Finally, average element counts of various µXRF element maps in none-pore pixels

16

386   (retrieved from segmented µXRF chlorine maps (Fig. 1e) were calculated as a

387   function of root distance (retrieved from registered 3D distance maps) with ImageJ

388   (Fig. 6). R version 3.53 (Team 2013) and the libraries readxl, stringr, and ggplot were

389   used to create Fig. 1f and Fig. 6b. All figures are compiled with CorelDraw 2018

390   (Corel Corporation).

3. Results and Discussion

391

392   *Imaging of 2D radial gradients*

393   The outlined correlative imaging approach was applied to planted soil columns

394   repeatedly scanned by X-ray CT, which informed on the root development with

395   weekly resolution and enabled targeted subsampling directly after harvest of the

396   three weeks old plant (Fig. 1a). The subsample for which correlative microscopy was

397   demonstrated was centered on a primary root being at least 14 days old and

398   including laterals of the same age (Fig. 1b). The prolonged root-soil interaction

399   around the investigated primary root resulted in a Ca accumulation gradient in the

400   rhizosphere with a spatial extent of ~200 µm that was detected by µXRF (Fig. 1f, Fig.

401   6). A gradient of the same spatial extent was detected for S. Even though the

402   speciation cannot be analysed with µXRF, the matching gradients suggest the

403   precipitation of gypsum ($CaSO_4 \cdot 2H_2O$) around the primary root. A possible reason

404   could be supply of Ca and S by the soil was greater than the uptake by the roots with

405   the consequence that mass flow was the primary mechanism for the supply of Ca

406   and S to the root surface, which would be consistent with experimental observations

407   by Oliveira et al. [42]. As reported by Ahmed et al. [43] water uptake of *Zea mays* L.

408   depends on root type. Therefore a different range of gradients can presumably be

17

409   observed for younger roots and other root types. Precipitation of gypsum in the

410   rhizosphere has also been reported for substrates with high concentrations of Ca and

411   SO_4 in the soil solution [3]. Likewise Hinsinger et al. [6] observed an enrichment of

412   water-extractable Ca in direct vicinity of roots when Ca-containing rock phosphate

413   was added to alumina sand planted with clover or ryegrass. Using synchroton-based

414   X-ray absorption near edge structure spectroscopy, Veelen et al. [44] found an

415   increase of Fe oxides, such as FeO and Fe_2O_3 as well as a three-fold increase of

416   inorganic sulfate (SO_4^{2-}) in the direct proximity of the root. With µXRF we could

417   potentially detect all elements heavier than sodium, including the macronutrient

418   phosphorus (P). Unlike for Ca and S, there was no gradient formation visible for P

419   when analysed by µXRF, despite of significant P uptake into maize plants [16]. This

420   can be explained by matrix effects causing high background noise level [45] and small

421   X-ray yield, thus leading to low P sensitivity. Nevertheless, some patches of larger P

422   accumulation, potentially related to abundant P-bearing minerals or remnants of the

423   fertilizer, could be observed (images not shown).

424   For the investigated rhizosphere transect we found by LA-IRMS that ^{13}C

425   enrichment occurred even at distant soil locations up to 100 µm away from the direct

426   root-soil interface (Fig. 4b). This finding accords with recent observations of

427   rhizosphere distances >100 µm that have been detected with LA-IRMS in resin

428   embedded topsoil samples from a Miscanthus field [24]. The NanoSIMS maps (Fig. 4)

429   revealed that these deviations from the baseline δ^{13}C values of the bulk soil in LA-

430   IRMS spots are caused by small areas of high enrichment that only comprise a small

431   fraction of the laser spot, possibly reflecting ^{13}C bound to specific mineral surfaces or

432   contained in soil microorganisms like bacteria (Fig. 4a). Mycorrhiza are also known to

433   transport ^{13}C to distant soil locations [27,46] but plants in our experiment showed only

18

434   minor signs of mycorrhizal colonization [16]. Because of the patchy appearance of ^{13}C

435   enrichment up to the penultimate spot of the transect, we conclude an even longer

436   transect would have been necessary to completely capture the enrichment zone

437   around the primary root. This would be in line with the predictions of a modeling

438   approach by Landl et al. [47] suggesting elevated concentrations of exudates (mucilage

439   and citrate) up to a distance of 250 µm for 10 and 15 day old *Vicia faba* roots.

440   Therefore, further investigation of targeted samples of other root types and ages is

441   necessary to picture ^{13}C release into the soil.

442   In addition to ^{13}C measurements it was also possible to map the spatial

443   distribution of ^{15}N with NanoSIMS (Fig. 4a). We observed ^{15}N in various distinct areas

444   within the soil matrix, potentially reflecting individual ^{15}N-enriched microorganisms [28],

445   but most pronounced ^{15}N enrichment occurred in the root tissue (Fig. 4a). As there

446   was no gradual transition between high and low ^{15}N enrichment areas, we speculate

447   that some of the initial NO_3-N label was partially removed during the embedding

448   procedure.

449   In summary, each 2D imaging technique used in the presented workflow has specific

450   advantages and limitations and hence provides complementary information at

451   different scales. Microscopic imaging methods generally determine only total element

452   concentrations that are not necessarily related to concentration in soil solution or the

453   empirically determined plant-available fractions obtained with specific extractants.

454   This is of particular relevance for elements with only a small plant-available fraction in

455   relation to total concentration as it is typically the case for P [48]. With µXRF only

456   relative differences between samples of different parent materials can be

457   investigated. A quantification of absolute element contents per area with µXRF would

458   be possible but requires a large number of reference samples and standards or a

459   complex calculation based on the assumption that all elements in the sample were

460   detected. For quantification of element contents per soil weight other methods based

461   on destructive sampling would have to be added into the sampling cascade.

462   However, such measurements would be incompatible with the non-destructive

463   assessment of 3D rhizosphere properties. While current approaches with rhizoboxes

464   or root windows allow quantification of mass-based element contents [7], they

465   generally lack the spatial 3D information which we can tackle with our targeted

466   mapping approach.

467   We also showed that small-scale information on the fate of ^{13}C and ^{15}N at the

468   single cell level can be derived from NanoSIMS measurements (field of view of 30 ×

469   30 µm with a resolution of 0.12 µm) in order to provide a qualitative picture of C and

470   N allocations patterns brought about by plant-microbe-soil interactions for a limited

471   number of locations (Fig. 4a) [27,28]. In contrast to NanoSIMS, LA-IRMS is able to map

472   larger transects of δ^{13}C with lower costs at a spot size of 30 µm (Fig. 4b). It is the

473   only truly quantitative method in the presented workflow and as such can quantify C

474   allocation patterns in the rhizosphere. Correlative imaging of NanoSIMS and LA-

475   IRMS therefore provides some added benefits: First, NanoSIMS can inform why

476   specific isotope enrichment was observed with LA-IRMS, e.g. small-scale variability

477   can be related to varying area fractions of enriched cell wall residues or varying

478   number of microorganisms per spot area (Fig. 4c). Second, LA-IRMS can be

479   harnessed to calibrate qualitative information on isotope ratios with quantitative δ^{13}C

480   values. This is possible because the laser spot size roughly matches the spatial

481   dimensions of the NanoSIMS images resulting in very good agreement between LA-

482   IRMS readings and average ^{13}C enrichment (arithmetic mean of 256 × 256 pixels) in

483   NanoSIMS images (R²=0.82, n=11, p<0.001; Fig. 4d).

20

484   In addition to our workflow Bandara et al [37] developed a workflow which is

485   suitable to identify bacteria in undisturbed soil. On a similar set of samples Lohse et

486   al. [49] presented a workflow using mass resolution laser desorption ionization Fourier-

487   transform ion cyclotron resonance mass spectrometry for the direct analysis of the

488   molecular gradients in the rhizosphere. Our workflow can be used with the mentioned

489   approaches as they complement each other and result in a more holistic picture of

490   rhizosphere processes.

491   *Structural integrity*

492   To the best of our knowledge, there is no study to date that systematically examines

493   the structural changes during the fixation and embedding procedure. Here we could

494   show that the combination of dehydration with acetone and resin embedding with

495   araldite under mild vacuum leads to minimal structural deformation. Dehydration as a

496   necessary condition for vacuum stability is a prerequisite for a lot of techniques like

497   NanoSIMS or LA-IRMS. Preservation of original root-soil contact is essential to

498   calculate correct distances from the soil to the root surface which could be only

499   estimated in other studies [44]. A fixation of the root after sampling is a necessary step

500   in this workflow, as root shrinkage can occur before sampling because of drought

501   stress [50]; assuming a perfect root-soil contact in air-dried samples can therefore lead

502   to misinterpretation of results. To preserve the structural integrity, we decided to

503   dehydrate the samples in a series of acetone additions. The chemical gradients

504   observed with correlative imaging might therefore represent conservative estimates

505   of the true rhizosphere extent as easily soluble compounds might have been partially

506   washed out. This wash-out effect was also reduced by only partially saturating the

507   subsamples with fixative through capillary rise instead of full immersion (Fig. 3).

508   Furthermore, unsaturated subsamples showed a better structural stability during the

509   second X-ray CT scan at 10 µm resolution as any movement of an unconsolidated

510   soil fully saturated with liquid inevitably leads to settling of the subsample.

511   *Registration of 2D radial gradients in 3D context*

512   The combination of 3D structural and 2D chemical information is crucial to represent

513   the radial geometry of accumulation and depletion zones around roots. Calculating

514   root distance maps on a 2D plane can lead to a bias because information about roots

515   outside of the microscopy plane is missing. The direct comparison of root distance

516   maps which are based on the 2D microscopy (Fig. 5b) to distance maps calculated

517   for the whole 3D image stack (Fig. 5c) show that for distances in the range of up to

518   ~200 µm there were hardly any differences. That is, for the detected gradients (Ca

519   and S with µXRF, ^{13}C with NanoSIMS and LA-IRMS) in this study the discrepancy

520   between apparent 2D and real 3D root distances are irrelevant for the findings. In

521   other words, the risk of missing an even closer, hidden root is low in the direct vicinity

522   of a visible root. However, in more distant areas considering true 3D distances can

523   reduce any uncertainty related to roots that come close to the soil sections, but do

524   not touch it. A direct comparison of 2D and 3D root distances shows that this is not

525   the case for this particular subsample (Fig. 5).

526   To sum up, targeted sampling enables to determine chemical rhizosphere gradients

527   for root segments of known type and age. With this sampling method at hand the

528   temporal development of gradients can be addressed in the future, i.e. it will be

529   possible to investigate how quickly element gradients develop and how long they last

530   after root activity fainted. Combination of 3D and 2D information overcomes a

531   prominent artefact of rhizobox systems. Information on root activity above and below

22

532   the analysed plane is available and can be used for data interpretation by ruling out

533   the uncertainty brought about by hidden roots. Overcoming the second major artefact

534   of rhizoboxes – growth along a solid plane with altered properties as compared to soil

535   – comes at a prize. It is possible to perform chemical imaging for soil-grown roots

536   and the root-soil contact can be maintained by a careful protocol of sample

537   extraction, fixation, and embedding. However, smearing of original gradients by the

538   infiltration of the fixative and embedding medium cannot be fully ruled out. The

539   patchy appearance of small-scale gradients measured with our workflow, which is

540   obviously related to the size of individual soil particles, expresses not only the

541   necessity of systematic measurements done with a sufficient number of biological

542   replicates but also that with the given resolution one has to move from the concept of

543   continuum scale to pore scale processes.

544

Author Contributions

546   ELI carried out the growth experiment, preparation of thin slices was done by ELI and

547   GH, ELI and RK carried out the µXRF measurements, CH performed NanoSIMS, MG

548   and ELE where responsible for LA-IRMS measurements. DV and SS acquired the

549   funding and did the conceptualization, RM acquired the funding for µXRF, ELI and

550   SS carried out the correlative imaging, ELI wrote the first draft of the manuscript. The

551   manuscript was written through contributions of all authors. All authors have given

552   approval to the final version of the manuscript.

23

Acknowledgements

Disclosures

The authors declare no competing financial interest.

24

References

(1)   Stubbs, C. J.; Cook, D. D.; Niklas, K. J. A General Review of the Biomechanics of Root Anchorage. *J. Exp. Bot.* **2019**, *70* (14), 3439–3451. https://doi.org/10.1093/jxb/ery451.

(2)   Cai, G.; Ahmed, M. A.; Abdalla, M.; Carminati, A. Root Hydraulic Phenotypes Impacting Water Uptake in Drying Soils. *Plant Cell Environ.* **2022**, *45* (3), 650–663. https://doi.org/10.1111/pce.14259.

(3)   Hinsinger, P. *How Do Plant Roots Acquire Mineral Nutrients? Chemical Processes Involved in the Rhizosphere*; Elsevier Masson SAS, 1998; Vol. 64. https://doi.org/10.1016/S0065-2113(08)60506-4.

(4)   Vetterlein, D.; Lippold, E.; Schreiter, S.; Phalempin, M.; Fahrenkampf, T.; Hochholdinger, F.; Marcon, C.; Tarkka, M.; Oburger, E.; Ahmed, M.; Javaux, M.; Schlüter, S. Experimental Platforms for the Investigation of Spatiotemporal Patterns in the Rhizosphere—Laboratory and Field Scale. *J. Plant Nutr. Soil Sci.* **2021**, *184* (1), 35–50. https://doi.org/10.1002/jpln.202000079.

(5)   Darrah, P. R. The Rhizosphere and Plant Nutrition: A Quantitative Approach. *Plant Soil* **1993**, *155–156* (1), 1–20. https://doi.org/10.1007/BF00024980.

(6)   Hinsinger, P.; Gilkes, R. J. Mobilization of Phosphate from Phosphate Rock and Alumina-Sorbed Phosphate by the Roots of Ryegrass and Clover as Related to Rhizosphere PH. *Eur. J. Soil Sci.* **1996**, *47* (4), 533–544. https://doi.org/10.1111/j.1365-2389.1996.tb01853.x.

(7)   Bilyera, N.; Hummel, C.; Daudin, G.; Santangeli, M.; Zhang, X.; Santner, J.; Lippold, E.; Schlüter, S.; Bertrand, I.; Wenzel, W.; Spielvogel, S.; Vetterlein, D.; Razavi, B. S.; Oburger, E. Co-Localised Phosphorus Mobilization Processes in

25

587   the Rhizosphere of Field-Grown Maize Jointly Contribute to Plant Nutrition. *Soil*

588   *Biol. Biochem.* **2022**, *165*, 108497.

589   https://doi.org/10.1016/j.soilbio.2021.108497.

590 (8) Kuzyakov, Y.; Razavi, B. S. Rhizosphere Size and Shape: Temporal Dynamics

591   and Spatial Stationarity. *Soil Biol. Biochem.* **2019**, *135* (May), 343–360.

592   https://doi.org/10.1016/j.soilbio.2019.05.011.

593 (9) Norvell, W. A.; Cary, E. E. Potential Errors Caused by Roots in Analyses of

594   Rhizosphere Soil. *Plant Soil* **1992**, *143* (2), 223–231.

595   https://doi.org/10.1007/BF00007877.

596 (10) Vetterlein, D.; Carminati, A.; Kögel-Knabner, I.; Bienert, G. P.; Smalla, K.;

597   Oburger, E.; Schnepf, A.; Banitz, T.; Tarkka, M. T.; Schlüter, S. Rhizosphere

598   Spatiotemporal Organization–A Key to Rhizosphere Functions. *Front. Agron.*

599   **2020**, *2* (July). https://doi.org/10.3389/fagro.2020.00008.

600 (11) Roose, T.; Keyes, S. D.; Daly, K. R.; Carminati, A.; Otten, W.; Vetterlein, D.;

601   Peth, S. Challenges in Imaging and Predictive Modeling of Rhizosphere

602   Processes. *Plant Soil* **2016**, *407* (1–2), 9–38. https://doi.org/10.1007/s11104-

603   016-2872-7.

604 (12) Göttlein, A.; Heim, A.; Matzner, E. Mobilization of Aluminium in the

605   Rhizosphere Soil Solution of Growing Tree Roots in an Acidic Soil. *Plant Soil*

606   **1999**, *211* (1), 41–49. https://doi.org/10.1023/A:1004332916188.

607 (13) Dessureault-Rompré, J.; Nowack, B.; Schulin, R.; Luster, J. Modified Micro

608   Suction Cup/Rhizobox Approach for the in-Situ Detection of Organic Acids in

609   Rhizosphere Soil Solution. *Plant Soil* **2006**, *286* (1–2), 99–107.

610   https://doi.org/10.1007/s11104-006-9029-z.

611 (14) Werner, L. M.; Knott, M.; Diehl, D.; Ahmed, M. A.; Banfield, C.; Dippold, M.;

  26

612   Vetterlein, D.; Wimmer, M. A. Physico-Chemical Properties of Maize (Zea Mays

613   L.) Mucilage Differ with the Collection System and Corresponding Root Type

614   and Developmental Stage of the Plant. *Plant Soil* **2022**, No. 0123456789.

615   https://doi.org/10.1007/s11104-022-05633-9.

616 (15) Vetterlein, D.; Doussan, C. Root Age Distribution: How Does It Matter in Plant

617   Processes? A Focus on Water Uptake. *Plant Soil* **2016**, *407* (1–2), 145–160.

618   https://doi.org/10.1007/s11104-016-2849-6.

619 (16) Lippold, E.; Phalempin, M.; Schlüter, S.; Vetterlein, D. Does the Lack of Root

620   Hairs Alter Root System Architecture of Zea Mays ? *Plant Soil* **2021**, No.

621   0123456789. https://doi.org/10.1007/s11104-021-05084-8.

622 (17) Pflugfelder, D.; Kochs, J.; Koller, R.; Jahnke, S.; Mohl, C.; Pariyar, S.;

623   Fassbender, H.; Nagel, K. A.; Watt, M.; Van Dusschoten, D. The Root System

624   Architecture of Wheat Establishing in Soil Is Associated with Varying

625   Elongation Rates of Seminal Roots: Quantification Using 4D Magnetic

626   Resonance Imaging. *J. Exp. Bot.* **2022**, *73* (7), 2050–2060.

627   https://doi.org/10.1093/jxb/erab551.

628 (18) Schlüter, S.; Eickhorst, T.; Mueller, C. W. Correlative Imaging Reveals Holistic

629   View of Soil Microenvironments. *Environ. Sci. Technol.* **2019**, *53* (2), 829–837.

630   https://doi.org/10.1021/acs.est.8b05245.

631 (19) Hapca, S.; Baveye, P. C.; Wilson, C.; Lark, R. M.; Otten, W. Three-Dimensional

632   Mapping of Soil Chemical Characteristics at Micrometric Scale by Combining

633   2D SEM-EDX Data and 3D X-Ray CT Images. *PLoS One* **2015**, *10* (9).

634   https://doi.org/10.1371/journal.pone.0137205.

635 (20) Keyes, S.; van Veelen, A.; McKay Fletcher, D.; Scotson, C.; Koebernick, N.;

636   Petroselli, C.; Williams, K.; Ruiz, S.; Cooper, L.; Mayon, R.; Duncan, S.;

27

637   Dumont, M.; Jakobsen, I.; Oldroyd, G.; Tkacz, A.; Poole, P.; Mosselmans, F.;

638   Borca, C.; Huthwelker, T.; Jones, D. L.; Roose, T. Multimodal Correlative

639   Imaging and Modelling of Phosphorus Uptake from Soil by Hyphae of

640   Mycorrhizal Fungi. *New Phytol.* **2022**, *234* (2), 688–703.

641   https://doi.org/10.1111/nph.17980.

642 (21) Juyal, A.; Otten, W.; Falconer, R.; Hapca, S.; Schmidt, H.; Baveye, P. C.;

643   Eickhorst, T. Combination of Techniques to Quantify the Distribution of

644   Bacteria in Their Soil Microhabitats at Different Spatial Scales. *Geoderma*

645   **2019**, *334* (February 2018), 165–174.

646   https://doi.org/10.1016/j.geoderma.2018.07.031.

647 (22) Kravchenko, A. N.; Guber, A. K.; Razavi, B. S.; Koestel, J.; Blagodatskaya, E.

648   V.; Kuzyakov, Y. Spatial Patterns of Extracellular Enzymes: Combining X-Ray

649   Computed Micro-Tomography and 2D Zymography. *Soil Biol. Biochem.* **2019**,

650   *135* (June), 411–419. https://doi.org/10.1016/j.soilbio.2019.06.002.

651 (23) Lucas, M.; Pihlap, E.; Steffens, M.; Vetterlein, D.; Kögel-Knabner, I.

652   Combination of Imaging Infrared Spectroscopy and X-Ray Computed

653   Microtomography for the Investigation of Bio- and Physicochemical Processes

654   in Structured Soils. *Front. Environ. Sci.* **2020**, *8* (April), 1–12.

655   https://doi.org/10.3389/fenvs.2020.00042.

656 (24) Rodionov, A.; Lehndorff, E.; Stremtan, C. C.; Brand, W. A.; Königshoven, H.-

657   P.; Amelung, W. Spatial Microanalysis of Natural 13 C/ 12 C Abundance in

658   Environmental Samples Using Laser Ablation-Isotope Ratio Mass

659   Spectrometry. *Anal. Chem.* **2019**, *91* (9), 6225–6232.

660   https://doi.org/10.1021/acs.analchem.9b00892.

661 (25) Zaeem, M.; Nadeem, M.; Huong Pham, T.; Ashiq, W.; Ali, W.; Shah Mohioudin

662   Gillani, S.; Moise, E. R. D.; Leier, H.; Kavanagh, V.; Galagedara, L.; Cheema,

663   M.; Thomas, R. Development of a Hyperspectral Imaging Technique Using LA-

664   ICP-MS to Show the Spatial Distribution of Elements in Soil Cores. *Geoderma*

665   **2021**,   *385*   (November   2020),   114831.

666   https://doi.org/10.1016/j.geoderma.2020.114831.

667   (26)   Possinger, A. R.; Zachman, M. J.; Enders, A.; Levin, B. D. A.; Muller, D. A.;

668   Kourkoutis, L. F.; Lehmann, J. Organo–Organic and Organo–Mineral Interfaces

669   in Soil at the Nanometer Scale. *Nat. Commun.* **2020**, *11* (1), 1–11.

670   https://doi.org/10.1038/s41467-020-19792-9.

671   (27)   Vidal, A.; Hirte, J.; Bender, S. F.; Mayer, J.; Gattinger, A.; Höschen, C.;

672   Schädler, S.; Iqbal, T. M.; Mueller, C. W. Linking 3D Soil Structure and Plant-

673   Microbe-Soil Carbon Transfer in the Rhizosphere. *Front. Environ. Sci.* **2018**, *6*

674   (February), 1–14. https://doi.org/10.3389/fenvs.2018.00009.

675   (28)   Clode, P. L.; Kilburn, M. R.; Jones, D. L.; Stockdale, E. A.; Cliff, J. B.;

676   Herrmann, A. M.; Murphy, D. V. In Situ Mapping of Nutrient Uptake in the

677   Rhizosphere Using Nanoscale Secondary Ion Mass Spectrometry. *Plant*

678   *Physiol.* **2009**, *151* (4), 1751–1757. https://doi.org/10.1104/pp.109.141499.

679   (29)   Rohde, F.; Braumann, U. D.; Schmidt, M. Correlia: An ImageJ Plug-in to Co-

680   Register and Visualise Multimodal Correlative Micrographs. *J. Microsc.* **2020**,

681   *280* (1), 3–11. https://doi.org/10.1111/jmi.12928.

682   (30)   Védère, C.; Vieublé Gonod, L.; Nunan, N.; Chenu, C. Opportunities and Limits

683   in Imaging Microorganisms and Their Activities in Soil Microhabitats. *Soil Biol.*

684   *Biochem.* **2022**, *174*, 108807. https://doi.org/10.1016/j.soilbio.2022.108807.

685   (31)   Phalempin, M.; Lippold, E.; Vetterlein, D.; Schlüter, S. Soil Texture and

686   Structure Heterogeneity Predominantly Governs Bulk Density Gradients

687   around   Roots.   *Vadose   Zo.   J.*   **2021**,   No.   July.

688   https://doi.org/10.1002/vzj2.20147.

689   (32)   Heinrich, S.; Dippold, M. A.; Werner, C.; Wiesenberg, G. L. B.; Kuzyakov, Y.;

690   Glaser, B. Allocation of Freshly Assimilated Carbon into Primary and

691   Secondary Metabolites after in Situ 13C Pulse Labelling of Norway Spruce

692   (Picea   Abies).   *Tree   Physiol.*   **2015**,   *35*   (11),   1176–1191.

693   https://doi.org/10.1093/treephys/tpv083.

694   (33)   Lippold, E.; Kleinau, P.; Blaser, S. R. G. A.; Schlüter, S.; Phalempin, M.;

695   Vetterlein, D. In Soil Measurement of Radiation Dose Caused by X-Ray

696   Computed   Tomography.   *J.   Plant   Nutr.   Soil   Sci.*   **2021**,   1–3.

697   https://doi.org/10.1002/jpln.202000276.

698   (34)   Karnovsky, M. A Formaldehyde-Glutaraldehyde Fixative of High Osmolality for

699   Use in Electron Microscopy. *J. Cell Biol.* **1965**, *27*, 137-138A.

700   (35)   Mueller, C. W.; Kölbl, A.; Hoeschen, C.; Hillion, F.; Heister, K.; Herrmann, A.

701   M.; Kögel-Knabner, I. Submicron Scale Imaging of Soil Organic Matter

702   Dynamics Using NanoSIMS – From Single Particles to Intact Aggregates. *Org.*

703   *Geochem.*   **2012**,   *42*   (12),   1476–1488.

704   https://doi.org/10.1016/j.orggeochem.2011.06.003.

705   (36)   Herrmann, A. M.; Clode, P. L.; Fletcher, I. R.; Nunan, N.; Stockdale, E. A.;

706   O'Donnell, A. G.; Murphy, D. V. A Novel Method for the Study of the

707   Biophysical Interface in Soils Using Nano-Scale Secondary Ion Mass

708   Spectrometry. *Rapid Commun. Mass Spectrom.* **2007**, *21* (1), 29–34.

709   https://doi.org/10.1002/rcm.2811.

710   (37)   Bandara, C. D.; Schmidt, M.; Davoudpour, Y.; Stryhanyuk, H.; Richnow, H. H.;

711   Musat,   N.   Microbial   Identification,   High-Resolution   Microscopy   and

Spectrometry of the Rhizosphere in Its Native Spatial Context. *Front. Plant Sci.* **2021**, *12* (July), 1–18. https://doi.org/10.3389/fpls.2021.668929.

(38) Holz, M.; Leue, M.; Ahmed, M. A.; Benard, P.; Gerke, H. H.; Carminati, A. Spatial Distribution of Mucilage in the Rhizosphere Measured with Infrared Spectroscopy. *Front. Environ. Sci.* **2018**, *6* (AUG), 1–7. https://doi.org/10.3389/fenvs.2018.00087.

(39) Poczatek, C.; Kaufman, Z.; Lechene, C. *OpenMIMS ImageJ Plugin Guide*. http://nrims.harvard.edu/files/nrims/files/openmims-manual.pdf.

(40) Schindelin, J.; Arganda-Carreras, I.; Frise, E.; Kaynig, V.; Longair, M.; Pietzsch, T.; Preibisch, S.; Rueden, C.; Saalfeld, S.; Schmid, B.; Tinevez, J. Y.; White, D. J.; Hartenstein, V.; Eliceiri, K.; Tomancak, P.; Cardona, A. Fiji: An Open-Source Platform for Biological-Image Analysis. *Nat. Methods* **2012**, *9* (7), 676–682. https://doi.org/10.1038/nmeth.2019.

(41) Klein, S.; Staring, M.; Murphy, K.; Viergever, M. A.; Pluim, J. P. W. Elastix: A Toolbox for Intensity-Based Medical Image Registration. *IEEE Trans. Med. Imaging* **2010**, *29* (1), 196–205. https://doi.org/10.1109/TMI.2009.2035616.

(42) Oliveira, E. M. M.; Ruiz, H. A.; Alvarez V, V. H.; Ferreira, P. A.; Costa, F. O.; Almeida, I. C. C. Nutrient Supply by Mass Flow and Diffusion to Maize Plants in Response to Soil Aggregate Size and Water Potential. *Rev. Bras. Ciência do Solo* **2010**, *34* (2), 317–328. https://doi.org/10.1590/S0100-06832010000200005.

(43) Ahmed, M. A.; Zarebanadkouki, M.; Meunier, F.; Javaux, M.; Kaestner, A.; Carminati, A. Root Type Matters: Measurement of Water Uptake by Seminal, Crown, and Lateral Roots in Maize. *J. Exp. Bot.* **2018**, *69* (5), 1199–1206. https://doi.org/10.1093/jxb/erx439.

31

737 (44) Veelen, A. Van; Koebernick, N.; Scotson, C. S.; Mckay-fletcher, D.;

738   Huthwelker, T.; Borca, C. N.; Mosselmans, J. F. W.; Roose, T. Root-Induced

739   Soil Deformation Influences Fe , S and P : Rhizosphere Chemistry Investigated

740   Using Synchrotron XRF and XANES. **2019**, No. 2010.

741   https://doi.org/10.1111/nph.16242.

742 (45) Mukhtar, S.; Haswell, S. J.; Ellis, A. T.; Hawke, D. T. Application of Total-

743   Reflection X-Ray Fluorescence Spectrometry to Elemental Determinations in

744   Water, Soil and Sewage Sludge Samples. *Analyst* **1991**, *116* (4), 333.

745   https://doi.org/10.1039/an9911600333.

746 (46) Witzgall, K.; Vidal, A.; Schubert, D. I.; Höschen, C.; Schweizer, S. A.; Buegger,

747   F.; Pouteau, V.; Chenu, C.; Mueller, C. W. Particulate Organic Matter as a

748   Functional Soil Component for Persistent Soil Organic Carbon. *Nat. Commun.*

749   **2021**, *12* (1), 1–10. https://doi.org/10.1038/s41467-021-24192-8.

750 (47) Landl, M.; Haupenthal, A.; Leitner, D.; Kroener, E.; Vetterlein, D.; Bol, R.;

751   Vereecken, H.; Vanderborght, J.; Schnepf, A. Simulating Rhizodeposition

752   Patterns around Growing and Exuding Root Systems. *In Silico Plants* **2021**, *3*

753   (2), 1–14. https://doi.org/10.1093/insilicoplants/diab028.

754 (48) Kruse, J.; Abraham, M.; Amelung, W.; Baum, C.; Bol, R.; Kühn, O.;

755   Lewandowski, H.; Niederberger, J.; Oelmann, Y.; Rüger, C.; Santner, J.;

756   Siebers, M.; Siebers, N.; Spohn, M.; Vestergren, J.; Vogts, A.; Leinweber, P.

757   Innovative Methods in Soil Phosphorus Research: A Review. *J. Plant Nutr. Soil*

758   *Sci.* **2015**, *178* (1), 43–88. https://doi.org/10.1002/jpln.201400327.

759 (49) Lohse, M.; Haag, R.; Lippold, E.; Vetterlein, D.; Reemtsma, T.; Lechtenfeld, O.

760   J. Direct Imaging of Plant Metabolites in the Rhizosphere Using Laser

761   Desorption Ionization Ultra-High Resolution Mass Spectrometry. *Front. Plant*

32

762   *Sci.* **2021**, *12* (December), 1–13. https://doi.org/10.3389/fpls.2021.753812.

763   (50) Carminati, A.; Vetterlein, D.; Koebernick, N.; Blaser, S.; Weller, U.; Vogel, H. J.

764   Do Roots Mind the Gap? *Plant Soil* **2013**, *367* (1–2), 651–661.

765   https://doi.org/10.1007/s11104-012-1496-9.

766

767

768

Tables

770 Table 1: Sequence, required sample preparation steps and purpose of X-ray CT, light
771 microscopy, µXRF, SEM, NanoSIMS, and LA-IRMS fulfilled within the correlative
772 imaging workflow
773

| technique	sample preparation	purpose
X-ray CT	- targeted sampling	- track changes after resin impregnation - determine root distances
light microscopy	- targeted sampling - chemical fixation	- reference image for orientation and image registration of all image data
µXRF	- dehydration - resin impregnation - thin sectioning	- elemental mapping of nutrients - pore detection with Cl channel - particle detection with Si channel
SEM	- targeted sampling - chemical fixation	- reference image for orientation and image registration of NanoSIMS
NanoSIMS	- dehydration - resin impregnation - thin sectioning - sputter coating with Au/Pd layer	- isotope mapping of $^{16}O^-$, $^{12}C^{12}C^-$, $^{12}C^{13}C^-$ $^{12}C^{14}N^-$, $^{12}C^{15}N^-$, $^{27}Al^{16}O^-$ - qualitative interpretation of LA-IRMS transects
LA-IRMS	- targeted sampling - chemical fixation - dehydration - resin impregnation - thin sectioning	- quantitative $\delta^{13}C$ transects
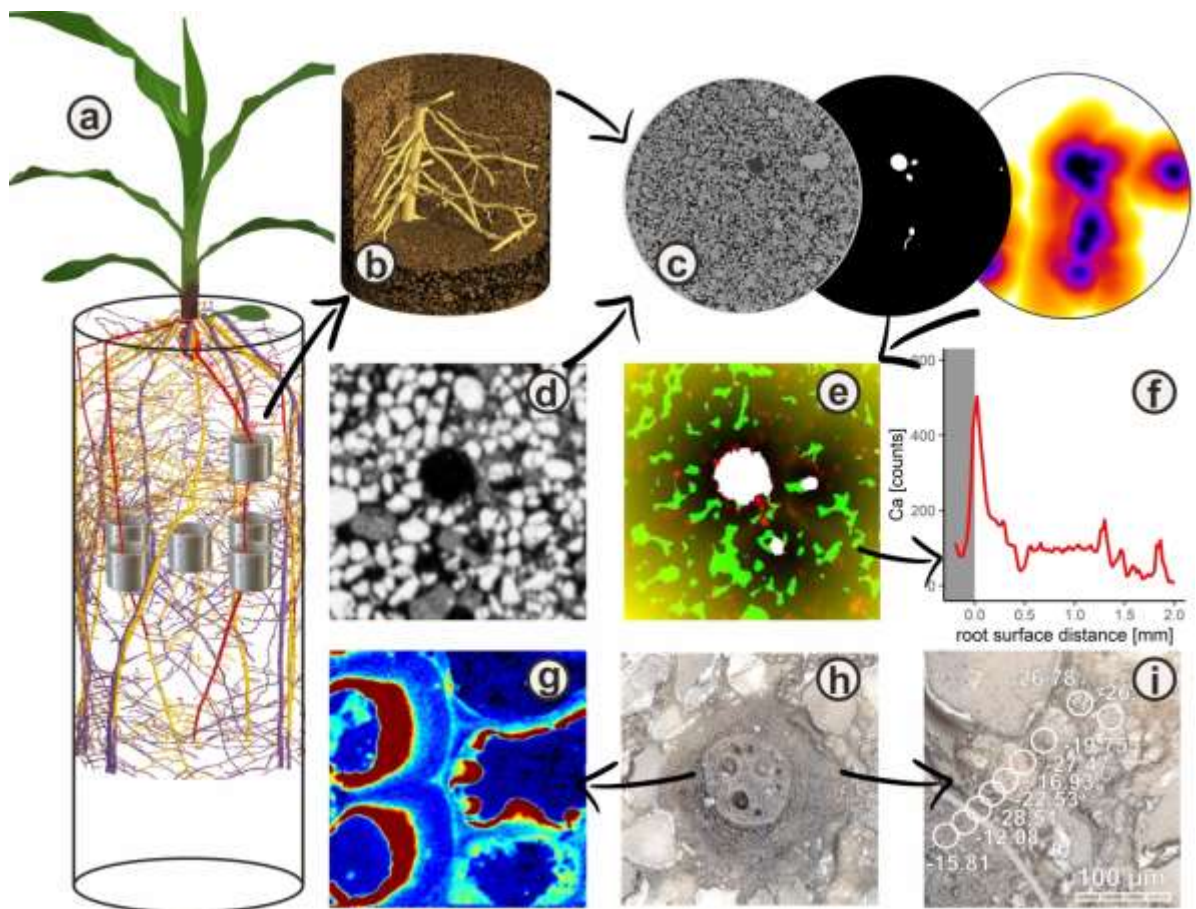
Figures

Figure 1: Workflow for imaging of radial 2D chemical rhizosphere gradients in a 3D structural context, all images show the same sample with sandy substrate: a) segmented root system, red: at least 14-day old roots, yellow: up to 14-day old roots, purple: up to 7-day old roots; cylinders in upper row show targeted position of a sample around the primary root; cylinders in the middle show untargeted sampling approach; b) targeted sample of primary root showing segmented root system; c) Image analysis of 2D imaging slice including raw image, root segmentation and root distance; d) µXRF Si channel which is registered into 3D context; e) image stack of µXRF images showing Ca channel (red) and Cl channel (green, representing resin filled pores excluded from following image analysis), root mask (white), Euclidean distances to the root surface (yellow); f) Ca counts as a function of root distance; g) NanoSIMS image of root tissue (focusing on the endodermis with casparian band) showing ^{13}C ratio ($^{12}C^{13}C^{-}$:$^{12}C^{2-}$), natural abundance (blue) up to high enriched areas (red); h) brightfield microscope image of primary root, and i) LA-IRMS transect

790 registered onto brightfield image, circles indicate ablation spots, numbers refer to
791 δ^{13}C at ablated spots.

792
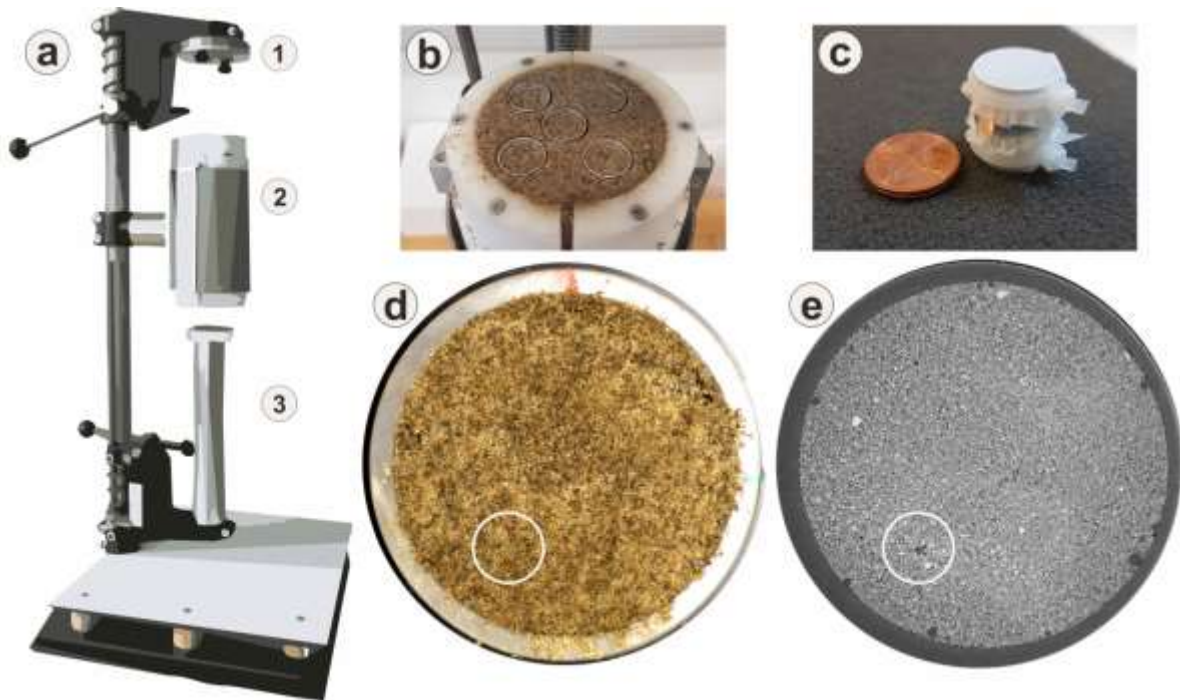
793
794
795 Figure 2: a) Device for extraction of subsamples with 1) specimen mount for non-
796 targeted sampling of subsamples from soil columns, 2) specimen mount for soil
797 column, and 3) moveable punch to push the soil out of the column; b) non-targeted
798 soil sampling; c) sample with mesh and cable tie; d) top-view on the soil surface of
799 the whole soil column with selection for targeted sampling in the sandy substrate; e)
800 X-ray CT image of the same soil slice as shown in (d) with selection for targeted
801 sampling showing the primary root.

802
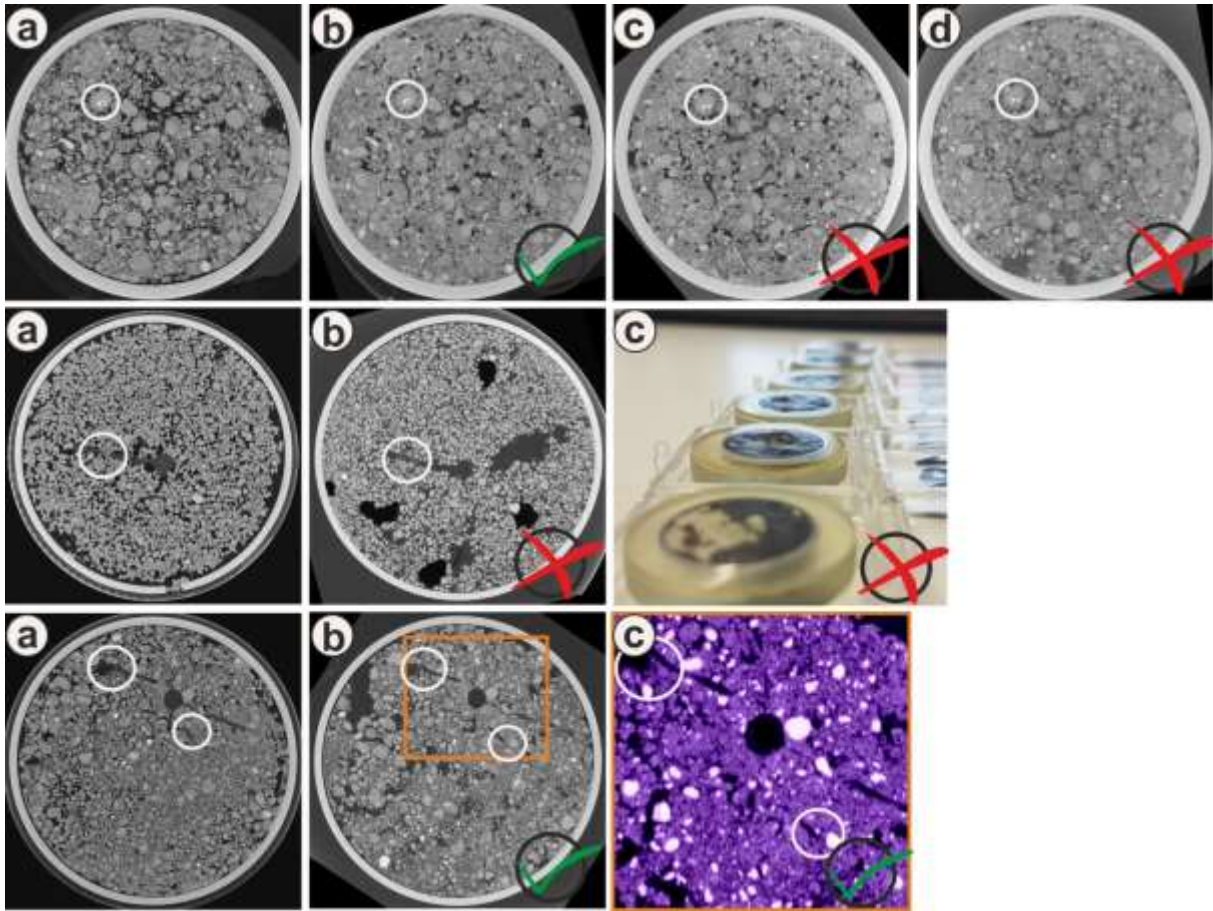
Figure 3: Examples of best practise and failures during sample fixation, embedding, slicing, and polishing. White circles show landmarks for orientation within X-ray CT images unless otherwise stated. **Upper row**: a) undisturbed soil structure; b) soil after partial saturation through capillary rise after partial immersion into fixative; c) soil after almost full immersion into fixative (only top 1 mm reaches out of fixative); d) soil exposed to strong vacuum under boiling of fixative at 30 mbar for 5 min. **Middle row**: a) undisturbed soil sample with primary root and lateral root in sand; b) same soil after resin impregnation; c) photo of visible deformation because of outgassing during hardening and too strong vacuum during resin impregnation. **Last row**: a) undisturbed soil sample with primary root and lateral root; b) same soil sample after resin impregnation with almost no relocation of particles; c) co-registered µXRF image of the Si channel.

37
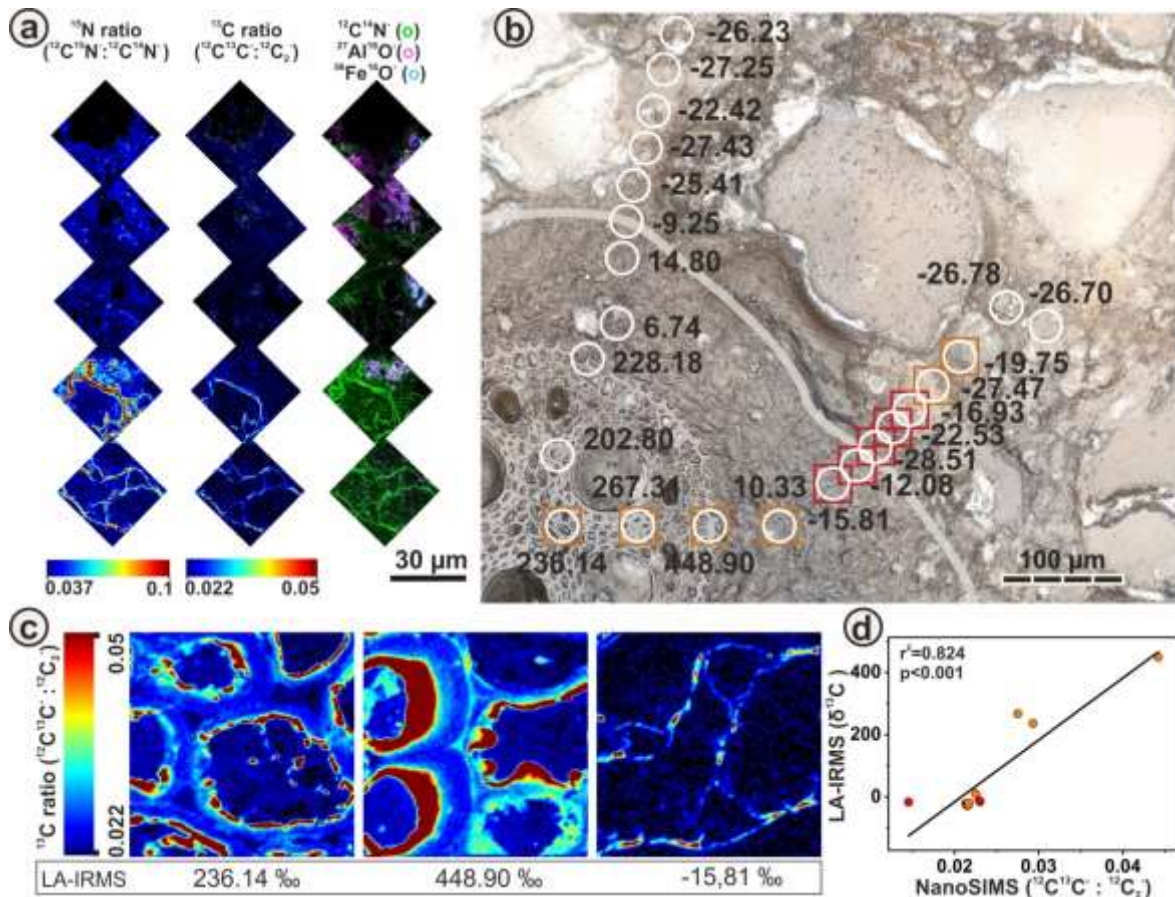
Figure 4: a) NanoSIMS results of ^{15}N and ^{13}C isotopic ratios of the transect marked by red rectangles in (b) and composite images of ^{12}C^{14}N$^-$ (green), ^{27}Al^{16}O$^-$ (magenta), and ^{65}Fe^{16}O$^-$ (cyan) secondary ions showing root tissue of primary root (bottom), rhizosphere, and mineral matrix of sandy substrate (top); b) light microscopy image with the root-soil interface indicated by the white line. White circles show LA-IRMS spots registered on brightfield microscopy image with corresponding δ^{13}C values and red and orange rectangles indicate the NanoSIMS spots, red rectangles show the position of the NanoSIMS transect presented in (a); c) NanoSIMS images of root tissue and corresponding values of LA-IRMS measurements done at the same location show that ^{13}C enrichment barely varied because of locally different ^{13}C enrichment in cell walls, but because of randomly varying cell wall area fractions covered in each LA-IRMS spot; d) correspondence between average ^{13}C enrichment in a NanoSIMS map (arithmetic mean of all 256 x 256 pixels) and the ^{13}C enrichment in a co-localized LA-IRMS spot (r^2=0.82, p<0.001), red circles depict red rectangles in (b), the same accounts for orange circles.
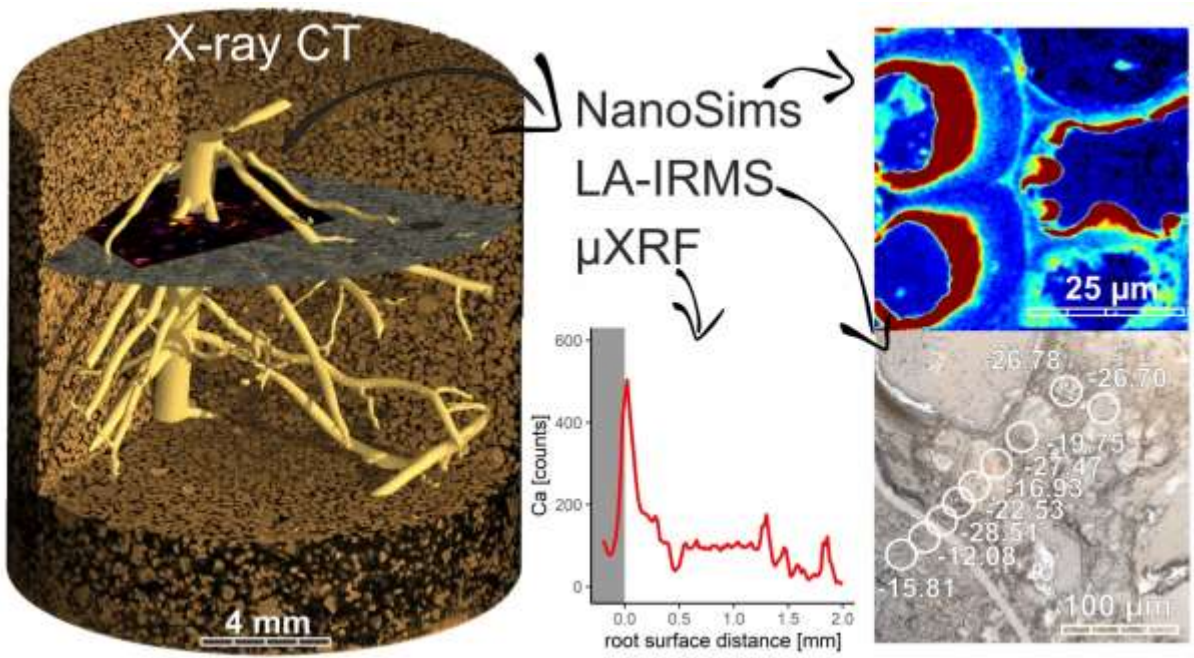
38
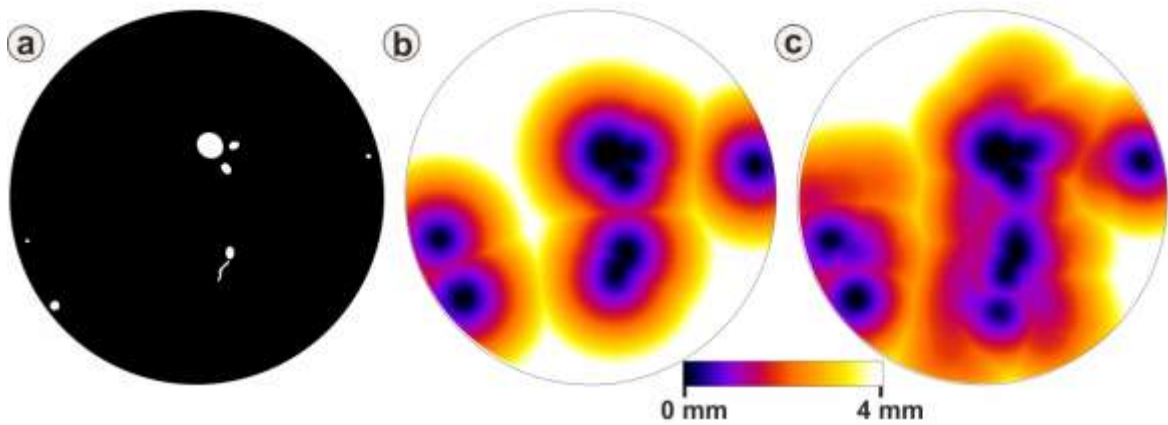
834

835 Figure 5: a) Slice of segmented co-registered root system; b) Euclidean distance
836 map (EDT) done on 2D image ignoring hidden roots outside of microscopy plane; c)
837 EDT calculated on 3D image so that roots outside the microscopy plane are
838 accounted for.

839
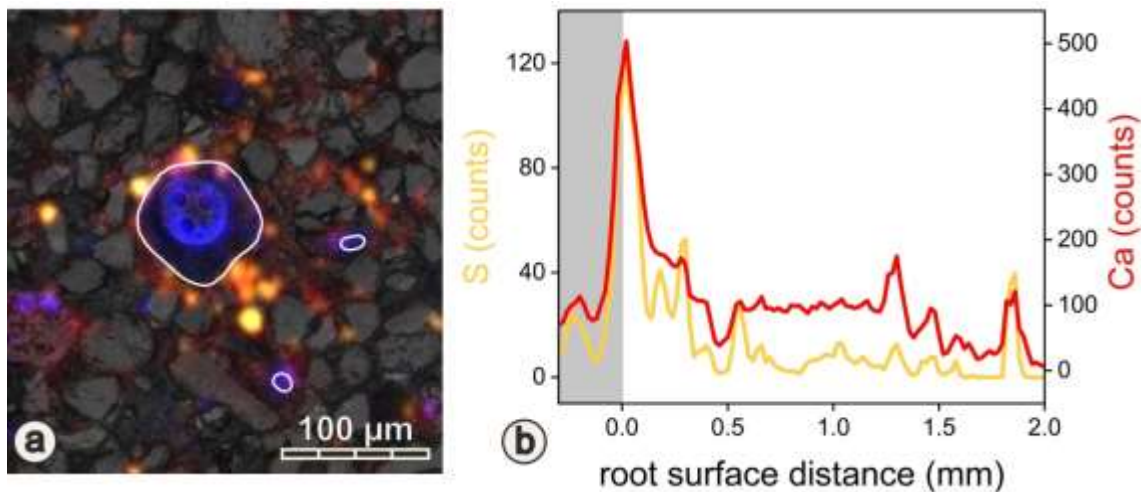
840

841

842 Figure 6: a) Light microscopy image with co-registered µXRF image of phosphor
843 (blue), sulphur (yellow), and calcium (red). White lines in µXRF image represent the
844 root-soil interface of primary root and laterals of the primary root. Note, the bright
845 blue circle indicating high phosphorus concentrations is spatially associated with the
846 endodermis and not with the root-soil interface; b) Calcium (Ca) and sulphur (S)
847 counts with increasing distance from the root surface are shown as well as Ca counts
848 from the root surface into the centre of the root (grey).

849

39

850   For Table of Contents Only

851

852